

## Spatio-temporal diffusion of dynamic PET images

This article has been downloaded from IOPscience. Please scroll down to see the full text article.

2011 Phys. Med. Biol. 56 6583

(<http://iopscience.iop.org/0031-9155/56/20/004>)

View [the table of contents for this issue](#), or go to the [journal homepage](#) for more

Download details:

IP Address: 147.127.100.21

The article was downloaded on 22/09/2011 at 09:14

Please note that [terms and conditions apply](#).

# Spatio-temporal diffusion of dynamic PET images

C Tauber<sup>1</sup>, S Stute<sup>2</sup>, M Chau<sup>3</sup>, P Spiteri<sup>4</sup>, S Chalon<sup>1</sup>,  
D Guilloteau<sup>1,5</sup> and I Buvat<sup>2</sup>

<sup>1</sup> Inserm U930, CNRS ERL3106, Université François Rabelais, Tours, France

<sup>2</sup> IMNC, IN2P3, UMR 8165 CNRS-Paris 7 and Paris 11 Universities, Orsay, France

<sup>3</sup> ASA—Advanced Solutions Accelerator, Montpellier, France

<sup>4</sup> IRIT—ENSEEIH, UMR CNRS 5505, Toulouse, France

<sup>5</sup> CHRU de Tours, Hôpital Bretonneau, Service de Médecine Nucléaire, Tours, France

E-mail: [clovis.tauber@univ-tours.fr](mailto:clovis.tauber@univ-tours.fr)

Received 17 June 2011, in final form 16 August 2011

Published 21 September 2011

Online at [stacks.iop.org/PMB/56/6583](http://stacks.iop.org/PMB/56/6583)

## Abstract

Positron emission tomography (PET) images are corrupted by noise. This is especially true in dynamic PET imaging where short frames are required to capture the peak of activity concentration after the radiotracer injection. High noise results in a possible bias in quantification, as the compartmental models used to estimate the kinetic parameters are sensitive to noise. This paper describes a new post-reconstruction filter to increase the signal-to-noise ratio in dynamic PET imaging. It consists in a spatio-temporal robust diffusion of the 4D image based on the time activity curve (TAC) in each voxel. It reduces the noise in homogeneous areas while preserving the distinct kinetics in regions of interest corresponding to different underlying physiological processes. Neither anatomical priors nor the kinetic model are required. We propose an automatic selection of the scale parameter involved in the diffusion process based on a robust statistical analysis of the distances between TACs. The method is evaluated using Monte Carlo simulations of brain activity distributions. We demonstrate the usefulness of the method and its superior performance over two other post-reconstruction spatial and temporal filters. Our simulations suggest that the proposed method can be used to significantly increase the signal-to-noise ratio in dynamic PET imaging.

(Some figures in this article are in colour only in the electronic version)

## 1. Introduction

Positron emission tomography (PET) can measure changes in the biodistribution of radiopharmaceuticals within organs of interest over time. Dynamic acquisitions associated

with kinetic modelling can yield physiological parameters characterizing the functional state of tissue. However, dynamic PET images suffer from high statistical noise that affects the quantitative accuracy of the parameters derived from compartmental modelling.

Spatial filtering methods have been proposed to reduce the noise in individual frames. Links *et al* (1992) proposed a high-frequency roll-off filter combined with the inverse of the transfer function in the Fourier space. Wavelet denoising was proposed by Lin *et al* (2001). More recently, anisotropic diffusion has been used in PET image reconstruction to incorporate anatomical priors (Chan *et al* 2009). Being based on the data from a single frame, these methods can reduce noise but they do not take advantage of the temporal consistency of the signal. In dynamic PET imaging, they can penalize spatial resolution and bias quantitative analysis when the differences in activity between two regions of interest (ROI) and the noise amplitude are of the same order of magnitude.

Consequently, there has been an increasing interest for methods making use of the signal change over time. These methods fall into two categories: (i) reconstruction methods and (ii) post-reconstruction methods. One of the key ideas behind 4D reconstruction methods is to use smooth temporal basis functions rather than the rectangular pulse commonly used in most clinical studies (Rahmim *et al* 2009). These basis functions model the correlation between data from adjacent frames. They can be either model based (Meikle *et al* 1998) or based on interpolation (Nichols *et al* 2002, Li *et al* 2007) or data driven (Matthews *et al* 1997, Reader *et al* 2006). These methods demonstrated the improvement brought by modelling the correlation between time frames. Recently, E-spline wavelets have been proposed for spatio-temporal reconstruction as an alternative to B-splines (Verhaeghe *et al* 2008). Post-reconstruction methods have also been proposed to account for the temporal consistency of the images. Herholz (1988) proposed a Gaussian filter with an adaptive range based on the TAC differences. Christian *et al* (2010) used the information contained in a time-averaged frame to filter each individual frame and increase the signal-to-noise ratio (SNR). Wavelet denoising was first restrained to the time domain to improve the SNR in PET kinetic curves (Millet *et al* 2000). Wavelets were also used for denoising 3D images and for kinetic analysis performed on the wavelet transform of the dynamic frames (Turkheimer *et al* 1999, 2003, Alpert *et al* 2006). Iterative temporal smoothing was applied to dynamic PET data, assuming similarity between close time frames (Walledge *et al* 2004) or by fitting the data to a predefined kinetic model (Kadrmas and Gullberg 2001).

The proposed approach is a post-reconstruction vector-based robust anisotropic diffusion (VRAD). It aims at facilitating the segmentation and improving the SNR in dynamic PET images. Unlike previous 4D processing methods, it takes advantage of both the spatial and temporal consistencies of the data and does not require a prior kinetic model. After the description of the method (section 2), we assess its performance using numerical head phantoms in comparison with two other post-processing methods (section 3). Results are presented in section 4 and discussed in section 5.

## 2. Methods

### 2.1. Definitions

Let us denote  $\Lambda^0(X) : \mathbb{R}^3 \mapsto \mathbb{R}^K$  the dynamic PET image,  $\Omega \in \mathbb{R}^3$  the spatial 3D domain of  $\Lambda^0$ ,  $X$  a point in  $\Omega$  and  $K$  the number of frames in the PET image series. Let  $k$  ( $k \in \{1, 2, \dots, K\}$ ) be a time frame of the series,  $\Delta_k$  the duration of that frame and  $\Delta$  the

total duration of the acquisition. We denote by  $I_k^0$  the 3D PET image corresponding to the  $k$ th time frame:

$$\forall X \in \Omega, \Lambda^0(X) = (I_1^0(X), I_2^0(X), \dots, I_K^0(X)). \tag{1}$$

With these notations, vector  $\Lambda^0(X)$  is the time activity curve (TAC) at point  $X$  of the reconstructed PET image. We denote by  $V^+(X)$  the spatial neighbourhood of point  $X$ .

2.2. VRAD modelling

Our approach consists in a 3D diffusion of the vector-valued image obtained from the reconstruction of the entire 4D data, where the vector associated with each voxel corresponds to its TAC. We assume Neumann boundary conditions on the border of the image domain  $\partial\Omega$ . The diffusion problem, denoted  $P$ , is defined as follows:

$$(P) \begin{cases} \frac{\partial \Lambda}{\partial t} - \text{div}_K(c(|\nabla \Lambda|)\nabla \Lambda) = 0, & \text{everywhere in } \Omega, 0 < t \leq T, \\ \frac{\partial \Lambda}{\partial n} |_{\partial\Omega} = 0, & \forall t \in [0, T] \text{ (boundary conditions),} \\ \Lambda(x, y, z, 0) = \Lambda^0(x, y, z) = \Lambda^0(X), & \text{(initial conditions),} \end{cases} \tag{2}$$

where  $\Lambda(x, y, z, t)$  is the TAC of point  $X = (x, y, z)$  at diffusion time  $t$ ;  $T$  is the total diffusion time and  $n$  is the outward vector normal to  $\partial\Omega$ . The diffusion coefficient  $c$  is a non-negative function of the magnitude of the local vector gradient  $|\nabla \Lambda|$ ; we specifically tailor both for the dynamic PET.  $\nabla \Lambda$  is the  $K$  rows  $\times$  3 columns Jacobian matrix of  $\Lambda$  and  $\text{div}_K$  is the classical divergence operator  $(\frac{\partial f_x}{\partial x} + \frac{\partial f_y}{\partial y} + \frac{\partial f_z}{\partial z})$  applied to each component of  $\nabla \Lambda$  (in other words, to each line of the Jacobian matrix).

To measure the local vector geometry, we associate the following gradient vector norm:

$$\|\nabla \Lambda\| = \left[ \frac{1}{\Delta} \sum_{k=1}^K \Delta_k \|\nabla I_k\|^2 \right]^{1/2}, \tag{3}$$

where  $\|\nabla I_k\|$  is the  $L_2$  norm of the gradient of the scalar image  $I_k$ .  $\Delta_t$  is used as a weighting factor to account for the noise dependence on the duration of the frame acquisition.

2.3. Coefficient of diffusion

In the dynamic PET, a filtering process should be unbiased to preserve the activity measured in each frame. In the diffusion problem, this can be achieved by adopting the Neumann boundary conditions (Weickert 1998, Tauber et al 2010). It is also desirable that in a given frame, the diffusion process does not change the total radiotracer activity within each homogeneous region, which implies some constraints on the coefficient of diffusion.

Let  $V$  be a 3D region of the image bounded by  $S = \partial V$  and  $n$  be the outward vector normal to  $S$ . The divergence theorem applied to frame  $I_k$  leads to

$$\iiint_V \frac{\partial I_k}{\partial t} dV = \iiint_V \text{div}(c(|\nabla \Lambda|)\nabla I_k) dV = \iint_S c(|\nabla \Lambda|)\nabla I_k \cdot n dS. \tag{4}$$

Applying this result to all the frames of a dynamic PET image, this yields the following.

- (i) If  $V$  is set to the spatial image domain  $\Omega$ , then the symmetrical (Neumann) border conditions ensure that the dot product  $\nabla I_k \cdot n = 0$  on  $\partial V = S$ . Thus, no diffusion occurs through the image borders and the global energy is strictly preserved if the minimum–maximum principle is respected.

- (ii) When  $V$  represents any homogeneous region of the image, the intra-region energy is preserved if the coefficient of diffusion is zero on its border  $\partial V$ . Indeed, if  $c(\|\nabla\Lambda\|) = 0$  everywhere on  $\partial V = S$ , then  $\iiint_V \frac{\partial I_k}{\partial t} dV = \iint_S c(\|\nabla\Lambda\|) \nabla I_k \cdot n dS = 0$ , which ensures that the total activity within  $V$  remains constant over time.

Classical coefficients of diffusion (Perona and Malik 1990, Charbonnier *et al* 1997, Tchumperle and Deriche 2002) can take low values but never reach zero and therefore cannot strictly preserve intra-region energy along diffusion time. To avoid contamination between ROIs with different TAC profiles, the coefficient of diffusion is based on Tukey's biweight function (You *et al* 1996, Black *et al* 1998, Tauber and Spiteri 2010), which can reach zero value on the borders of image regions:

$$c(\|\nabla\Lambda\|) = \begin{cases} \left[1 - \left(\frac{\|\nabla\Lambda\|}{\lambda}\right)^2\right]^2 & \text{if } \|\nabla\Lambda\| \leq \lambda, \\ 0 & \text{elsewhere.} \end{cases} \quad (5)$$

#### 2.4. Scale parameter estimation

Controlling the process of anisotropic diffusion requires a precise edge detection via the definition of the scale parameter  $\lambda$ . This parameter measures the degree to which a voxel belongs to an edge by defining the distance beyond which two TACs represent different physiological processes. To avoid a user-dependent parameter setting, we present an automatic estimation of  $\lambda$  to identify the edges at each iteration. This  $\lambda$  estimation assumes that the majority of voxels is within homogeneous regions. Under this assumption, most distances between voxels are expected to be low. Voxels across edges can then be detected as their distance will appear as outlier among the set of distances. We thus consider the set  $\mathbf{D}$  of all the distances between neighbour pixels:

$$\mathbf{D} = \left\{ \left[ \frac{1}{\Delta} \sum_{k=1}^K \Delta_k |I_k(X_i) - I_k(X_j)|^2 \right]^{1/2}; i < j, X_i \in V^+(X_j) \right\}. \quad (6)$$

The  $Q_n$  estimator is given by (Rousseeuw and Croux 1993)

$$Q_n = d\{|D_i - D_j|; i < j\}_{(\eta)}, \quad (7)$$

which is the  $\eta$ th-order statistic of the interpoint distance  $|D_i - D_j|$  for  $i < j$ , where  $\eta = C_2^h$  and  $h = [N/2] + 1$ . The coefficient  $d = 2.2219$  is included to ensure no bias at convergence when data are Gaussian. To avoid any dependence on the size of the field of view, only voxels inside the head are considered. The selection is performed via a pre-processing step in which we automatically threshold the sum image of all dynamic PET frames by multiscale analysis as proposed by Mangin *et al* (1998) and Maroy *et al* (2008).

The observations are normalized as follows:

$$v_i = \frac{D_i - \text{med}(\mathbf{D})}{Q_n}, \quad (8)$$

where  $\text{med}(\mathbf{D})$  is the median of all the distances between TACs at the current iteration. The scale  $\lambda_s$  is defined by setting  $v_i = 1$ , as established by Rousseeuw and Leroy (1987) for robustly standardized data:

$$\lambda_s = Q_n + \text{med}(\mathbf{D}). \quad (9)$$

Note that parameters  $\lambda_s$  and  $\lambda$  have to be distinguished.

- $\lambda_s$  is the threshold above which a pixel is considered to be on a contour;
- $\lambda$  is the threshold above which the diffusion is totally stopped in the corresponding direction.

Let  $\Phi = c(\|\nabla\Lambda\|)\|\nabla\Lambda\|$  be the influence function of the diffusion process. The point where the influence of outliers first begins to decrease occurs when the derivative of the  $\Phi$ -function is zero, which should correspond to  $\lambda_s$  (Black *et al* 1998). Under this condition, diffusion will be strong when  $\|\nabla\Lambda\| \leq \lambda_s$ , which indicates a homogeneous region. The diffusion flow will progressively decrease thereafter, until it becomes totally nil when  $\|\nabla\Lambda\| \geq \lambda$ .

The relationship between  $\lambda_s$  and  $\lambda$  can thus be derived as

$$\Phi'(\|\nabla\Lambda\| = \lambda_s) = 0 \Leftrightarrow \left[ x \left( 1 - \frac{x^2}{\lambda^2} \right)^2 \right]_{\lambda_s}' = 0 \Leftrightarrow \lambda_s = \frac{\lambda}{\sqrt{5}}. \tag{10}$$

$\lambda$  can thus be deduced as

$$\lambda = \sqrt{5} (Q_n + \text{med}(\mathbf{D})). \tag{11}$$

### 2.5. Discretization

We solve the vectorized problem  $P$  as  $K$  coupled diffusion problems ( $P_k$ ) on univariate images  $I_k$ .

$$(P_k) \begin{cases} \frac{\partial I_k}{\partial t} - \text{div}(c(\|\nabla\Lambda\|)\nabla I_k) = 0, \text{ everywhere in } \Omega, 0 < t \leq T, \\ \frac{\partial I_k(x,y,z,t)}{\partial n} \Big|_{\partial\Omega} = 0, \quad \forall t \in [0, T] \text{ (boundary conditions),} \\ I_k(x, y, z, 0) = I_k^0(x, y, z), \text{ (initial conditions),} \end{cases} \tag{12}$$

where the positive coefficient of diffusion  $c(\|\nabla\Lambda\|) = c(x, y, z, t, I_1, I_2, \dots, I_K)$  depends on the intensities from all time frames  $I_1, I_2, \dots, I_K$ . At each iteration, the scale parameter  $\lambda$  and the coefficient of diffusion are estimated using all images. Diffusion is then iterated once on each frame separately, using the global coefficient of the diffusion matrix for all images, with an explicit scheme and a timestep set to  $\tau = 0.05$ :

$$I_k^{t+1}(X) = I_k^t(X) + \frac{\tau}{\sharp V^+(X)} \sum_{M \in V^+(X)} c(\|\nabla\Lambda_{X,M}^t\|) \nabla I_{k;X,M}^t, \tag{13}$$

where  $\sharp V^+(X)$  denotes the number of spatial neighbours of point  $X$ . In this study, VRAD was applied on 2D+t slices and four neighbours were considered. Finally,  $\nabla I_{k;X,M}^t = I_k^t(X) - I_k^t(M)$  is the gradient of the intensity of voxel  $X$  with respect to  $M$  in image  $I_k^t$  and

$$\|\nabla\Lambda_{X,M}^t\| = \left[ \frac{1}{\Delta} \sum_{k=1}^K \Delta_k (\nabla I_{k;X,M}^t)^2 \right]^{1/2} \tag{14}$$

is the corresponding vector gradient norm which measures the TAC differences between  $X$  and  $M$ .

### 3. Simulations and experimental study

#### 3.1. Simulations

3.1.1. *TAC simulation.* TACs were simulated according to the three-compartment model proposed by Kamasak *et al* (2005) and Maroy *et al* (2008). This model assumes a homogeneous vascular fraction in each region. The input function is denoted  $C_P$  and is given by

$$C_P(t) = \alpha_0[(\alpha_1 t - \alpha_2 - \alpha_3) \exp(-\lambda_1 t) + \alpha_2 \exp(-\lambda_2 t) + \alpha_3 \exp(-\lambda_3 t)]. \quad (15)$$

The kinetics of the tissue compartment  $i$ , denoted  $C_i$ , was computed as

$$C_i(t) = \left( \sum_{w=1}^3 [a_{i,w} \exp(-t/b_{i,w})] \right) * C_P(t), \quad (16)$$

where  $*$  denotes the convolution operator. Parameters  $\alpha_0, \alpha_1, \alpha_2, \alpha_3, \lambda_1, \lambda_2, \lambda_3, a_{i,w}$  and  $b_{i,w}$  are randomly set using the constraints proposed by Maroy *et al* (2008):  $\alpha_0 \in [1E4, 3E5]$ ,  $\alpha_1 \in [0, 0.8]$ ,  $\alpha_2 \in [0, 1 - \alpha_1]$ ,  $\alpha_3 = 1 - \alpha_1 - \alpha_2$ ,  $\lambda_1 \in [30, 45]$ ,  $\lambda_2 \in [\lambda_1, 180]$ ,  $\lambda_3 \in [\lambda_1, 180]$ ,  $\alpha_0 \times a_{i,w} \in [1E3, 3E7]$  and  $b_{i,w} \in [48, 120]$ .

3.1.2. *Image simulation.* GATE Monte Carlo simulations (Jan *et al* 2004, 2011) of Philips Gemini GXL PET 4D acquisitions were performed, using the Zubal head phantom as a voxelized brain source (Zubal *et al* 1994). This phantom consists in a labelled MR image with voxels of  $1.1 \times 1.1 \times 1.4 \text{ mm}^3$ . Six regions of the phantom were considered for the simulations: cerebellum, frontal lobes, occipital, thalamus, parietal lobes and the remaining parts of the head (called background), plus a seventh region with no activity corresponding to air around the head, as shown in figure 1(a). These regions constituted the ground truth for segmentation evaluation. We generated three sets of TACs and simulated the three corresponding dynamic sequences, hereafter called simulations 1, 2 and 3. Each of these sequences consisted in  $5 \times 30s$  followed by  $15 \times 60s$  dynamic frames. Activities of all ROIs were simulated according to equation (16). Examples of simulated TACs used in simulation 1 are presented in figure 1(b). The total number of coincidences for each time frame varied between 5 and 70 millions. No attenuation medium was used and therefore no correction for attenuation and scatter was included in the reconstruction. The reconstruction of dynamic PET images was performed with a fully 3D OSEM iterative method, using five iterations and eight subsets, into  $2.2 \times 2.2 \times 2.8 \text{ mm}^3$  voxels. Neither correction for randoms nor post-smoothing were used.

#### 3.2. Comparison of VRAD to other methods

3.2.1. *Anisotropic diffusion (AD).* The spatial anisotropic diffusion process proposed by Perona and Malik (1990) was implemented for each frame  $I_k$  separately. The following coefficient of diffusion was used:

$$c(s) = \left[ 1 + \left( \frac{s}{\sigma_A} \right)^2 \right]^{-1}, \quad (17)$$

where  $s$  is the local gradient of  $I_k$  and  $\sigma_A$  is a scale parameter. We used an explicit scheme with the same timestep used for VRAD ( $\tau = 0.05$ ). For each image, the number of iterations and  $\sigma_A$  were chosen manually to maximize the total SNR (see equation (20)) of the resulting image.

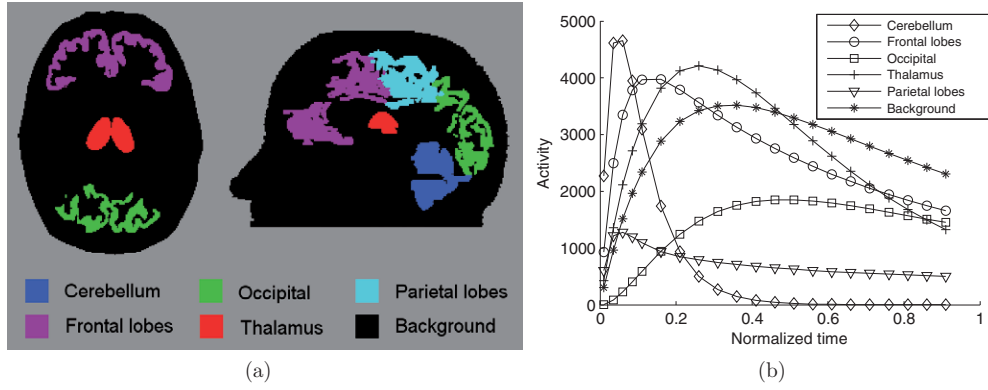


Figure 1. (a) ROIs used in the Zubal head phantom and (b) sample simulated TACs.

3.2.2. *Gaussian temporal filtering (GTF)*. All images were also convolved with the following low-pass Gaussian temporal kernel (Gundlich *et al* 2006):

$$g(t) = \frac{1}{\sqrt{2\pi}\sigma_G} \exp\left(-\frac{t^2}{2\sigma_G^2}\right), \quad (18)$$

where  $t$  is the temporal distance and  $\sigma_G$  is the temporal scale parameter. We used replicated temporal image borders. For each image sequence, the optimal scale parameter  $\sigma_G$  was chosen manually to maximize the total SNR (see equation (20)) of the resulting images.

### 3.3. Figures of merit

3.3.1. *Signal-to-noise ratio*. A SNR index was defined as

$$\text{SNR}_\Gamma(I_k) = \mu_\Gamma / \sigma_\Gamma, \quad (19)$$

where  $\Gamma$  is a homogeneous area manually drawn inside the phantom, far from the ROI borders, and  $\mu_\Gamma$  and  $\sigma_\Gamma$  are the mean and standard deviation of  $I_k$  over  $\Gamma$ . The same region  $\Gamma$  was used for all SNR calculations.

3.3.2. *Total SNR (TSNR)*. The SNR only considers a part of the image and does not measure the bias between ground truth values and estimated values. Therefore, we also used the TSNR (Gonzalez and Woods 2008) defined by

$$\text{TSNR}(I_k^{\text{res}}) = 10 \log_{10} \left( \frac{\|I_k^{\text{truth}}\|}{\|I_k^{\text{truth}} - I_k^{\text{res}}\|} \right)^2, \quad (20)$$

where  $I_k^{\text{truth}}$  is the piecewise constant ground truth image at frame  $k$ .  $I_k^{\text{truth}}$  was obtained by assigning to each ROI the mean value calculated over the same ROI in the image reconstructed without any filtering (called raw image thereafter).  $I_k^{\text{res}}$  is the  $k$ th frame of the 4D image resulting from a filtering process.

3.3.3. *Contrast*. Contrast was measured using entire frontal and background ROIs defined from the Zubal phantom labelling:

$$\text{Contrast} = 100 \cdot |\mu_{\text{bg}} - \mu_{\text{front}}| / \mu_{\text{bg}}, \quad (21)$$

where  $\mu_{\text{bg}}$  and  $\mu_{\text{front}}$  denote the mean intensity value within the background ROI and the frontal ROI. The Contrast versus TSNR was plotted for different numbers of iterations of the

filtering processes to observe the behaviour and convergence properties of the AD, GTF and VRAD methods.

**3.3.4. Pratt's figure of merit.** Pratt's figure of merit (PFOM) returns a number between 0 and 1 based upon the quality of the edge preservation and enhancement. PFOM is based on edge detection, localization and spurious responses. An automatic Canny edge detector from Matlab v2008b was applied on each image as a prior step for objective evaluation. The PFOM was then calculated as follows:

$$\text{PFOM}(I_k^{\text{res}}) = \frac{1}{\max(N_A, N_D)} \sum_{i=1}^{N_D} \frac{1}{1 + \alpha d_i^2}, \quad (22)$$

where  $N_A$  and  $N_D$  are respectively the number of the actual and detected edge voxels,  $d_i$  denotes the distance from the  $i$ th-detected edge voxel to the nearest actual edge voxel and  $\alpha$  is a scaling constant set to 1/9 as in Pratt's work (Pratt 1977).

**3.3.5. Root mean square error (RMSE).** The RMSE was defined as

$$\text{RMSE}(I_k^{\text{res}}) = \sqrt{\frac{1}{N} \sum_{X \in \Omega} [I_k^{\text{truth}}(X) - I_k^{\text{res}}(X)]^2}. \quad (23)$$

## 4. Results

### 4.1. Processed images

Figure 2 presents some results of AD, GTF and VRAD for three different simulations. All images were scaled to a common greyscale. The first two rows present a sagittal view of the fourth time frame of simulation 1, where all ROIs are visible. A visual comparison suggests that the level of noise and artefacts decreased when using VRAD for which ROIs are more homogeneous and almost as piecewise smooth as the ground truth. The thalamus has disappeared with AD because the uptake level was very close to that of the background. In contrast, it is still visible with GTF and VRAD both of which use the temporal information. Edges between ROIs are sharper with VRAD and AD than with GTF, and more precise with VRAD than with AD, indicating good edge detection. The middle and bottom rows in figure 2 present respectively an axial view of the 18th frame of simulation 2 and an axial view of the 13th frame of simulation 3. In both images, all structures are recovered with VRAD, especially the thalamus in simulation 2 and the frontal and occipital lobes in simulation 3. The result with VRAD is less biased compared to GTF in simulation 3, where GTF overestimates activity in the background region. This can also be seen in figure 2(d) where the cerebellum uptake is lower with GTF than in ground truth, while the activity is correctly recovered with VRAD (figure 2(e)). Once again, AD fails at preserving the differences in uptake between different ROIs. These trends are confirmed in figure 3 which presents 1D profiles of images shown in figures 2(f)–(j) along the line plotted in figure 2(f).

### 4.2. Quantitative criteria

Figure 4 presents the quantitative results obtained across all frames for the images presented in figures 2(b)–(e). Table 1 summarizes the quantitative results averaged over 300 images (5 slices  $\times$  3 simulations  $\times$  20 frames). Among the five slices, three were chosen in the transaxial plane and two in the sagittal plane. Three of them are shown in figure 2. They

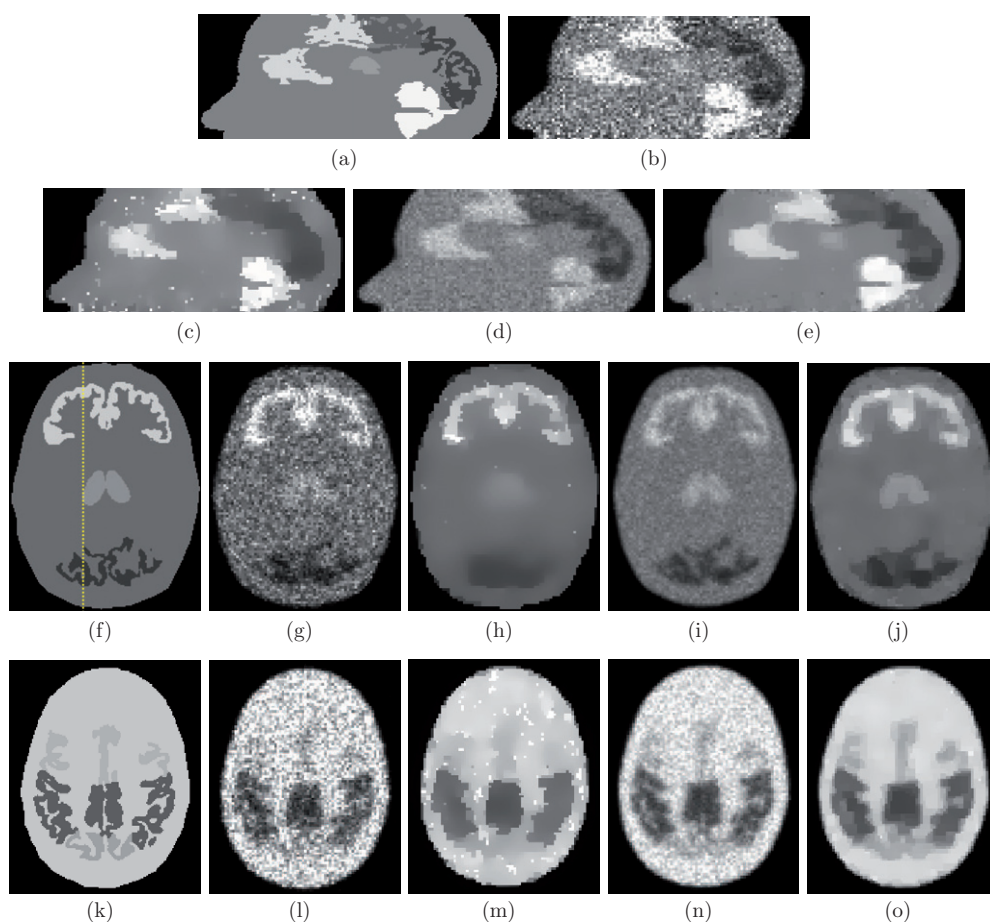


**Figure 2.** Sample views of the results obtained for three simulations. Top rows: the sagittal view of the results obtained for simulation 1: (a) ground truth, (b) raw image, (c) AD, (d) GTF, (e) VRAD. Middle row: transaxial view of the results obtained for simulation 2: (f) ground truth, (g) raw image, (h) AD, (i) GTF, (j) VRAD. Bottom row: transaxial view of the results obtained for simulation 3: (k) ground truth, (l) raw image, (m) AD, (n) GTF and (o) VRAD.

were chosen to contain several ROIs with different spatial arrangements. The SNR was highly increased with VRAD with an average SNR of 64.3 (see table 1), indicating strong smoothing of the noise within homogeneous areas. Results with AD and GTF lead to the average SNR of 12.4 and 12.1, respectively, while the SNR of the raw image was 4.1 on average. In contrast with the SNR, the TSNR is calculated over the entire field of view, better representing the overall quality of filtering. All three filters improve the quality of the image, with VRAD most increasing the TSNR from 10.6 to 15.7. The contrast was decreased with the three filters compared to the raw images. On average, the contrast was 39.0 with no post-processing, and 31.1, 33.4 and 35.4 with AD, GTF and VRAD, respectively. This decrease was expected as the three filters smooth the data. Figure 4(c) shows that the contrast varies along the frames of the dynamic sequence and that the variations are similar for the three filters. The edge detection and preservation measured with PFOM were the highest with VRAD. The average PFOM of raw images without post-reconstruction processing was 0.23, and increased by 35%,

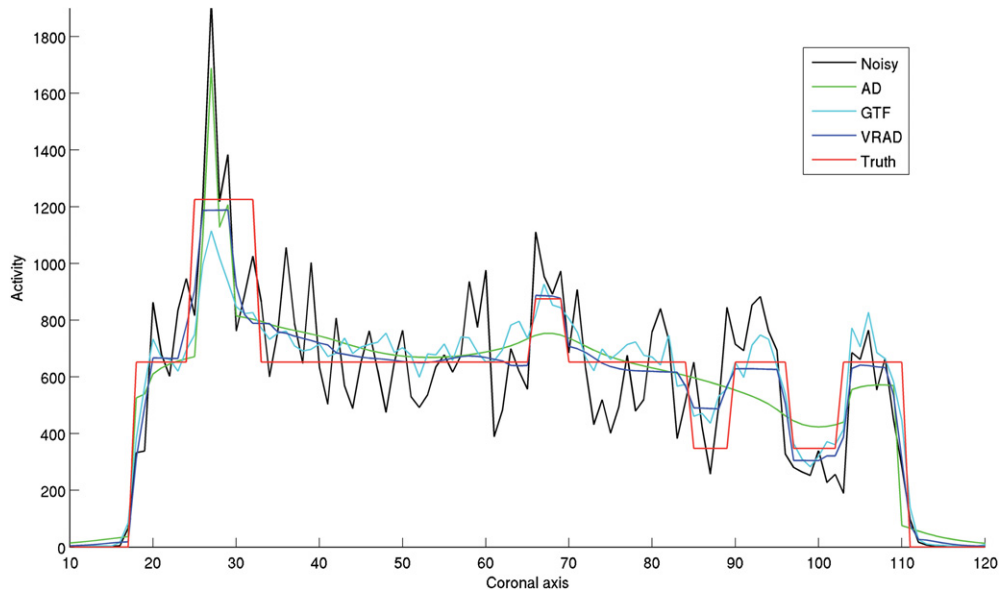


Figure 3. 1D profiles along the line drawn in figure 2(f).

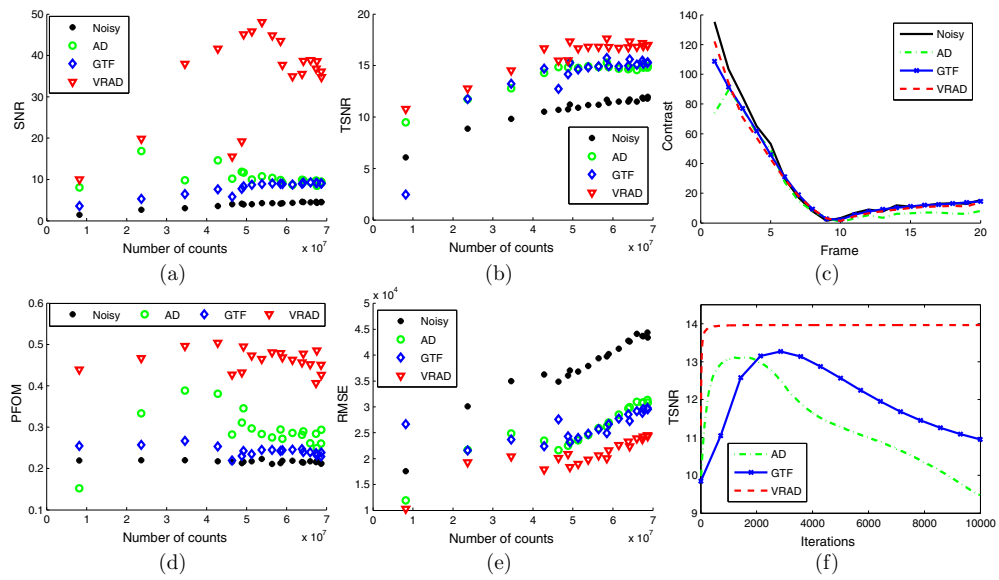
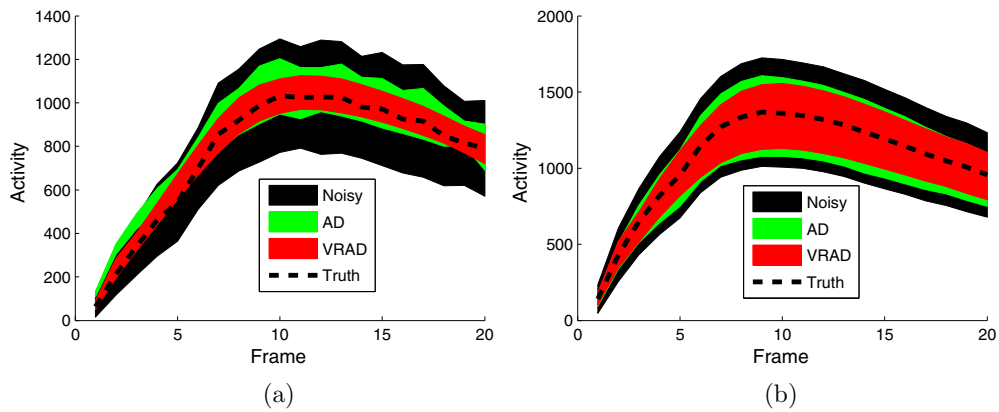


Figure 4. Quantitative criteria for all frames of simulation 1. (a) SNR, (b) TSNR, (c) contrast, (d) PFOM, (e) RMSE and (f) TSNR over 10000 iterations.

22% and 126% for AD, GTF and VRAD, respectively. On an average, the three filters reduced RMSE by a factor of 1.4, 1.4 and 1.9 with AD, GTF and VRAD, respectively.

The reduction of RMSE is further illustrated in figures 5(a) and (b), which respectively show the variability within the occipital lobes and background from simulation 3. The area



**Figure 5.** Areas covered by (mean $\pm$ sd) with AD, VRAD and without post-reconstruction processing in simulation 3. (a) Occipital lobes and (b) background.

**Table 1.** Figures of merit averaged over 300 images.

Method	SNR	TSNR (dB)	Contrast	PFOM	RMSE ( $\times 10^4$ )	CPU time (s)
Noisy	04.1	10.6	39.0	0.23	3.9	–
AD	12.4	13.9	31.1	0.31	2.7	11.5
GTF	12.1	14.0	33.4	0.28	2.7	07.8
VRAD	64.3	15.7	35.4	0.52	2.1	13.5

associated with AD, VRAD and the raw image corresponds to  $[\mu_{\text{ROI}} \pm \sigma_{\text{ROI}}]$ , where  $\mu_{\text{ROI}}$  is the mean uptake measured in the ROI and  $\sigma_{\text{ROI}}$  is the standard deviation. The result of GTF was not plotted for readability. In both figures, the ground truth TAC is plotted as a dashed line. VRAD filtering diminishes the variability of the TACs within both ROIs, while avoiding distortions that could introduce quantitative biases.

#### 4.3. Convergence

Figure 6 shows the joint evolution of contrast and TSNR along the iterative filtering processes. As in figure 4(f), both AD and VRAD were iterated 10000 times, while GTF was used with values of  $\sigma_G \in [0.5, 4.4]$ , expressed in minutes of acquisition. The point located at the bottom right corresponds to the contrast and TSNR of the raw image. For both AD and GTF, the TSNR first increases, reaches a maximum and then decreases, while the contrast decreases as the iteration number increases. Parameters involved in AD and GTF were manually set to obtain the maximum TSNR. The evolution with VRAD is very different as the TSNR always increases and converges to an upper bound. The contrast decreases but remains above a specific convergence value.

## 5. Discussion

The spatio-temporal anisotropic diffusion algorithm described in this paper is designed to improve the SNR in dynamic PET acquisitions, as a pre-processing step before kinetic modelling or image segmentation. VRAD is based on the TAC variations between voxels.

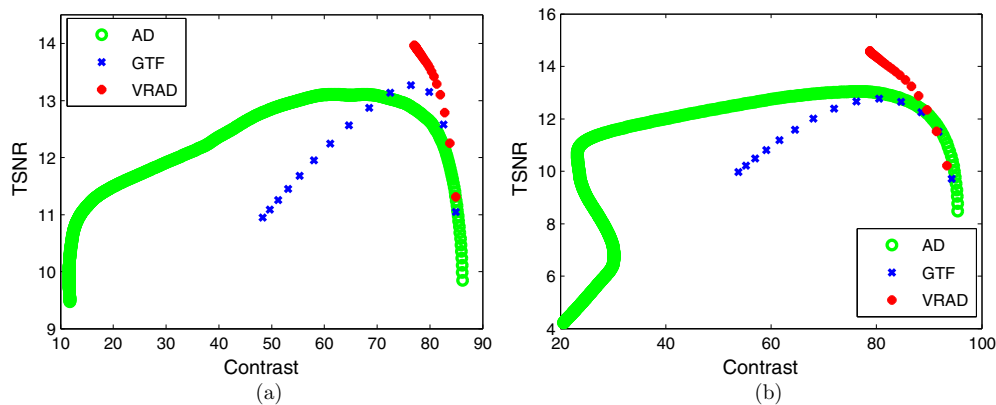


**Figure 6.** Contrast versus TSNR over 10000 iterations of AD, GTF and VRAD. (a) Simulation 1 and (b) simulation 3.

The smoothing is controlled by a coefficient of diffusion that accounts for the duration of each frame and which can prevent inter-ROIs TAC diffusion. VRAD does not include any assumption about the location of the functional structures. This avoids the use of possibly mismatched anatomical boundaries that might also not necessarily be relevant to the underlying biochemistry (Maroy *et al* 2008). The filtering is based on the entire temporal information available in each voxel to account for the underlying physiological processes rather than anatomical organs.

Due to the low spatial resolution and SNR, the main challenge in PET image filtering is to remove noise while preserving edges. In the proposed approach, the edges are detected by a statistical analysis of the distance between the voxel TACs. The scale parameter of the coefficient of diffusion is re-evaluated at each iteration to control the diffusion. The proposed coefficient of diffusion can not only reduce but also completely stop the diffusion across edges. As a consequence, it was demonstrated in section 2.3 that, under some conditions, VRAD preserves intra-region energy. This is especially relevant in dynamic PET images where inter-ROI filtering creates spill-over that introduces errors in quantitative analysis. This property of VRAD also explains its convergence behavior illustrated in figure 6. The diffusion is stopped between ROIs with different TACs; therefore, the method can maintain the contrast while improving the SNR. It converges towards an almost piecewise constant image in each frame. With conventional spatial anisotropic diffusion or Gaussian filtering, the filtering is never completely stopped and converge towards a homogeneous image. This property of VRAD adds more flexibility on the choice of number of iterations, as there is no risk to overdiffuse and miss the maximum of TSNR. This parameter can be adapted to the CPU time constraints. The estimation of the scale parameter requires the calculation of a  $Q_n$  estimator which represents a large part of the CPU time of VRAD. Alternatively, the median absolute deviation (MAD) can be used as a legitimate candidate for robust estimation instead of  $Q_n$  to reduce the computational time. We did not use MAD as it has some limitations (Rousseeuw and Croux 1993).

Partial volume effect affects PET imaging and can cause spill-over between regions (Soret *et al* 2007). The intra-region energy preservation of the proposed filtering scheme prevents additional spill-over but does not correct for PVE. However, VRAD can be used as a pre-processing step before PVE correction methods that rely on ROI definition (Rousset *et al*

1998). The fact that the PFOM increased with VRAD suggests that VRAD facilitates the detection of edges between ROIs.

The temporal filtering in VRAD is indirect: the diffusion occurs spatially in each frame which homogenizes the TACs within homogeneous regions. As the distance between voxels in VRAD is based on their TACs, it might benefit from prior mild temporal filtering methods that reduce noise. Therefore, VRAD is complementary with 4D reconstruction methods or iterative temporal filtering, as it can be used as a post-processing on any reconstructed dynamic PET image.

Like other time-based methods, VRAD is sensitive to motions that can occur during acquisition. Indeed, the TACs associated with voxels located near the interface of different functional regions would be a mixture of temporal profiles of the underlying tissues. Therefore, VRAD is not directly applicable for dynamic imaging of tissues affected by significant motion without prior motion correction.

Monte Carlo simulations of the Zubal brain phantom allowed us to perform a careful evaluation of the proposed approach for known activity maps. The results with VRAD compared favourably with two other filters. This validation would not have been possible on real data. The next step will consist in evaluating the impact of VRAD on even more realistic PET images and in patient images, and in determining how VRAD impacts the results of kinetic modelling in brain pathologies.

## 6. Conclusion

We have described an original VRAD spatio-temporal filtering scheme for dynamic PET imaging, based on the TACs of voxels. We introduced an automatic estimator of the scale parameter involved in the proposed diffusion method. Using PET brain images obtained from Monte Carlo simulations, we demonstrated that VRAD improved the SNR in dynamic PET images compared to spatial filtering or temporal filtering. As a result, VRAD appears as a promising pre-processing step before segmentation or quantitative analysis in clinical dynamic PET imaging of the brain.

## References

- Alpert N, Reilhac A and Chio T 2006 Optimization of dynamic measurement of receptor kinetics by wavelet denoising *Neuroimage* **30** 444–51
- Black M, Guillermo S and Marimont D 1998 Robust anisotropic diffusion *IEEE Trans. Image Process.* **7** 421–32
- Chan C, Fulton R, Feng D and Meikle S 2009 Regularized image reconstruction with an anatomically adaptive prior for positron emission tomography *Phys. Med. Biol.* **54** 7379–400
- Charbonnier P, Blanc-Feraud L, Aubert G and Barlaud M 1997 Deterministic edge-preserving regularization in computed imaging *IEEE Trans. Image Process.* **6** 298–311
- Christian B, Vandehey N, Floberg J and Mistretta C 2010 Dynamic PET denoising with HYPR processing *J. Nucl. Med.* **51** 1147–54
- Gonzalez R and Woods R 2008 *Digital Image Processing* (Englewood Cliffs, NJ: Prentice-Hall)
- Gundlich B, Musmann P and Weber S 2006 Dynamic list-mode reconstruction of PET data based on the ML-EM algorithm *IEEE Nucl. Sci. Symp. Conf. Rec.* **1** 2791–5
- Herholz K 1988 Non-stationary spatial filtering and accelerated curve fitting for parametric imaging with dynamic PET *Eur. J. Nucl. Med. Mol. Imaging* **14** 477–84
- Jan *et al* 2004 GATE: a simulation toolkit for PET and SPECT *Phys. Med. Biol.* **49** 4543–61
- Jan *et al* 2011 GATE V6: a major enhancement of the GATE simulation platform enabling modelling of CT and radiotherapy *Phys. Med. Biol.* **56** 881–901
- Kadrmas D and Gullberg G 2001 4D maximum a posteriori reconstruction in dynamic SPECT using a compartmental model-based prior *Phys. Med. Biol.* **51** 1553–74

- Kamasak M, Bouman C, Morris E and Sauer K 2005 Direct reconstruction of kinetic parameter images from dynamic PET data *IEEE Trans. Med. Imaging* **24** 636–50
- Li Q, Asma E, Ahn S and Leahy R 2007 A fast fully 4-D incremental gradient reconstruction algorithm for list mode PET data *IEEE Trans. Med. Imaging* **26** 58–67
- Lin J, Laine F and Bergmann S 2001 Improving PET-based physiological quantification through methods of wavelet denoising *IEEE Trans. Biomed. Eng.* **48** 202–12
- Links F, Leal J, Mueller-Gaertner H and Wagner H 1992 Improved positron emission tomography quantification by Fourier-based restoration filtering *Eur. J. Nucl. Med.* **19** 925–32
- Mangin J F, Coulon O and Frouin V 1998 Robust brain segmentation using histogram scale-space analysis and mathematical morphology *MICCAI Proc.* **1** 1230–41
- Maroy R *et al* 2008 Segmentation of rodent whole-body dynamic PET images: an unsupervised method based on voxel dynamics *IEEE Trans. Med. Imaging* **27** 342–54
- Matthews J, Bailey D, Price P and Cunningham V 1997 The direct calculation of parametric images from dynamic PET data using maximum likelihood reconstruction *Phys. Med. Biol.* **42** 1155–73
- Meikle S, Matthews J, Cunningham V, Bailey D, Liviteratos L, Jones T and Price P 1998 Parametric image reconstruction using spectral analysis of PET projection data *Phys. Med. Biol.* **43** 651–66
- Millet P *et al* 2000 Wavelet analysis of dynamic PET data: application to the parametric imaging of benzodiazepine receptor concentration *Neuroimage* **11** 458–72
- Nichols T, Qi J, Asma E and Leahy R 2002 Spatio-temporal reconstruction of list-mode PET data *IEEE Trans. Med. Imaging* **21** 396–404
- Perona P and Malik J 1990 Scale-space and edge detection using anisotropic diffusion *IEEE Trans. Pattern Anal. Mach. Intell.* **7** 629–39
- Pratt W 1977 *Digital Image Processing* (New York: Wiley)
- Rahmim A, Tang J and Zaidi H 2009 Four-dimensional (4D) image reconstruction strategies in dynamic PET: beyond conventional independent frame reconstruction *Med. Phys.* **36** 3654–70
- Reader A, Sureau F, Comtat C, Trebossen R and Buvat I 2006 Joint estimation of dynamic PET images and temporal basis functions using fully 4D ML-EM *Phys. Med. Biol.* **51** 5455–74
- Rousseeuw P and Leroy A 1987 *Robust Regression and Outlier Detection* (New York: Wiley)
- Rousseeuw P and Croux C 1993 Alternatives to the median absolute deviation *J. Am. Stat. Assoc.* **88** 1273–83
- Rousset O G, Ma Y and Evans A C 1998 Correction for partial volume effects in PET: principle and validation *J. Nucl. Med.* **39** 904–11
- Soret M, Bacharach S and Buvat I 2007 Partial-volume effect in PET tumor imaging *J. Nucl. Med.* **48** 932–45
- Tauber C and Spiteri P 2010 Ultrasound image filtering by anisotropic diffusion with numerical simulation *Adv. Med. Biol.* **25** 231–68
- Tauber C, Spiteri P and Batatia H 2010 Iterative methods for anisotropic diffusion of speckled medical images *Appl. Numer. Math.* **60** 1115–30
- Tchumperle D and Deriche R 2002 Diffusion PDE's on vector-valued images: local approach and geometric viewpoint *IEEE Signal Process. Mag.* **19** 16–25
- Turkheimer F, Brett M, Visvikis D and Cunningham V 1999 Multiresolution analysis of emission tomography images in the wavelet domain *J. Cereb. Blood Flow Metab.* **19** 1189–208
- Turkheimer F, Aston J, Banati R, Riddell C and Cunningham V 2003 A linear wavelet filter for parametric imaging with dynamic PET *IEEE Trans. Med. Imaging* **22** 289–301
- Verhaeghe J, Van De Ville D, Khalidov I, D'Asseler Y, Lemahieu I and Unser M 2008 Dynamic PET reconstruction using wavelet regularization with adapted basis functions *IEEE Trans. Med. Imaging* **27** 943–59
- Walledge R, Manavaki R, Honer M and Reader A 2004 Inter-frame filtering for list-mode EM reconstruction in high-resolution 4-D PET *IEEE Trans. Nucl. Sci.* **51** 705–11
- Weickert J 1998 *Anisotropic Diffusion in Image Processing* (Stuttgart: Teubner-Verlag)
- You Y, Xu W, Tannenbaum A and Kaveh M 1996 Behavioral analysis of anisotropic diffusion in image processing *IEEE Trans. Image Process.* **5** 1539–53
- Zubal G, Harrell C, Smith E, Rattner Z, Gindi G and Hoffer P 1994 Computerized three-dimensional segmented human anatomy *Med. Phys.* **21** 299–302